Lab on a Chip

PAPER

View Article Online
View Journal

Cite this: DOI: 10.1039/d5lc01095k

Monolithic 3D-printed split-and-recombine micromixer integrated into a microfluidic concentration gradient generator

Francisco Navarro Molina, [a] Jitendra Paliwal[b] and Elham Salimi *[a]

Received 26th November 2025,
Accepted 6th March 2026

DOI: 10.1039/d5lc01095k

rsc.li/loc

Efficient micromixing in enclosed microchannels is essential for reliable lab-on-a-chip operation but typically requires planar or multilayer soft-lithographic fabrication, limiting geometric freedom and increasing production complexity. Here, we report a fully monolithic split-and-recombine (SAR) micromixer fabricated in a single step using stereolithography digital light processing (SLA-DLP), eliminating molds, bonding, and cleanroom processing. The three-dimensional SAR architecture systematically divides, reorients, and recombines fluid streams, enabling high mixing performance over a wide range of operating conditions. Computational fluid dynamics simulations and experimental validation show excellent agreement, achieving mixing efficiencies above 0.90 across Reynolds numbers from 0.1 to 100. Leveraging its compact and robust performance, the micromixer was integrated into a five-output microfluidic concentration gradient generator, which produced stable and reproducible concentration profiles for both fluorescent tracers and protein solutions. The complete device, including microchannels and functional fluidic features, was printed in under 1.5 h using a standard desktop SLA-DLP system. These results demonstrate that additive manufacturing can deliver high-performance micromixing capabilities, establishing a rapid, accessible, and fully digital route for the fabrication of advanced microfluidic systems.

1. Introduction

Efficient mixing is a fundamental requirement in microfluidics, where laminar flow regimes dominate and diffusion alone is insufficient to achieve rapid homogenization. As a result, micromixers have become a cornerstone of microfluidic technology, enabling precise biochemical reactions, reproducible analytical assays, and sensitive diagnostic platforms.[1–5] In application domains such as drug screening, cell culture, and chemical analysis, the ability to generate well-defined and stable concentration profiles is critical, as it directly affects experimental reproducibility and the efficient use of limited reagents.[6–8]

To address the limitations of purely diffusive transport, a wide range of micromixer strategies has been developed over the past two decades. Passive micromixers, in particular, have attracted sustained interest because they rely exclusively on geometric features rather than external energy sources, making them simple, robust, and readily integrable into larger lab-on-a-chip systems.[9,10] Representative passive designs include the herringbone micromixer introduced by Stroock *et al.*, which induces chaotic advection through transverse secondary flows,[11] obstacle-based micromixers that perturb streamlines to enhance interfacial stretching,[12,13] and serpentine and zig-zag channels that increase residence time and elongate fluid interfaces.[14,15] Among these approaches split-and-recombine (SAR) architectures are particularly notable, as they systematically divide and reorient fluid streams to repeatedly reduce diffusion length scales, offering a scalable rout toward efficient mixing over a broad range of Re and channel geometries.[16,17]

Numerous SAR geometries have been proposed to minimize the diffusion length and mixing time under laminar flow conditions. Early planar or double-layer SAR designs, typically fabricated using soft lithography or deep reactive ion etching, demonstrated efficient mixing at low Re (<10),.[18,19] Subsequent variations including D-shaped sub-channels,[20] double-layer Y-type SAR structures,[19] and crossing or periodically interconnected junctions[21,22] improved interfacial stretching while reducing pressure drop, typically achieving complete mixing (ME $>$ 0.9) within channel lengths of 5–20 mm for Re $>$ 30. Multi-layer PDMS and silicon–glass hybrid devices[18] extended the operational Re range up to 100, while further geometric optimization, such as zigzag-angle tuning, broadened the effective operating window.[23] More recent studies have emphasized modular and scalable architectures, including a stackable SAR micromixer,[24] a "twisted" three-dimensional design,[25]

[a] Department of Electrical and Computer Engineering, University of Manitoba, Winnipeg, Manitoba, Canada. E-mail: elham.salimi@umanitoba.ca
[b] Department of Biosystems Engineering, University of Manitoba, Winnipeg, Manitoba, Canada

and the Y–Y micromixer,[19] a CNC-milled polycarbonate device employing alternating vertical ducts and planar Y-junctions, which achieve stable mixing (ME > 0.9) across wide Re range (1–100) with moderate pressure drop.

A comparative overview of SAR micromixers reported over the past decade is provided in Table 1, highlighting their materials, fabrication methods, characteristic dimensions, and operational ranges. The majority of reported SAR micromixers continue to rely on traditional photolithography and soft-lithography routes. Alternative manufacturing approaches, such as polymer lamination and xurography, have been explored to accelerate prototyping,[26] but these methods remain largely constrained to quasi-two-dimensional layouts. Consequently, fabrication complexity continues to limit both geometric freedom and scalability, motivating the exploration of more accessible and versatile manufacturing techniques for passive micromixers.[27,28] Additive manufacturing has recently emerged as a promising alternative for microfluidic device fabrication. More sophisticated three-dimensional structures have been realized using two-photon polymerization (2PP), particularly for printing molds for PDMS replication.[17] While such approaches can achieve excellent mixing performance in microchannels as small as 100 × 100 μm^2, they still rely on multistep soft-lithography workflows and indirect fabrication. In contrast stereolithography (SLA) 3D printing offers a combination of relatively high resolution, affordability, and the ability to directly fabricate enclosed internal channels with arbitrary three-dimensional configurations.[27,28] Beyond rapid prototyping, SLA 3D printing enables the integration of macro- and micro-scale features, such as ports, connectors, and reservoirs, within a single print, facilitating rapid iteration and increased functional complexity directly from digital models.

Despite the geometric freedom offered by SLA-based 3D printing, truly monolithic SAR micromixers fabricated in a single additive manufacturing step and comprehensively characterized over broad flow regimes remain largely unexplored. In particular, the incorporation of such micromixers into system-level microfluidic architectures has received limited experimental attention.

In this study, we present the design, numerical simulation, and experimental characterization of a fully 3D-printed SAR micromixer operating across a broad range of Re, along with its direct incorporation into a five-output microfluidic concentration gradient generator (MCGG) as a representative application. By embedding SAR micromixers within conventional "Christmas tree" and Y-junction network architectures, we fabricated a monolithic MCGG capable of producing five discrete, stable, and reproducible outlet concentrations over a wide range of flow conditions, which is particularly advantageous for high-throughput systems. The performance of the SAR micromixer and MCGG was evaluated through computational fluid dynamics (CFD) simulations and experimental measurements, confirming mixing uniformity and gradient reproducibility across Re ranging from 0.1 to 100. In addition, the fabrication process proved efficient and accessible, enabling complete device fabrication in under 1.5 hours using a mid-range SLA-DLP printer.

2. Materials and methods

2.1 Numerical Modeling

Numerical simulations were performed using COMSOL Multiphysics 6.2 (COMSOL, Inc., Burlington, Massachusetts, United States) to evaluate the performance of the SAR micromixer and the MCGG and optimize its design. The

Table 1 Comparative summary of split-and-recombine (SAR) micromixers or similar reported in recent literature. The table lists the fabrication method, material, Reynolds number range (Re) tested, channel dimensions, channel length, and corresponding references. ("n/r" stands for non-reported)

Fabrication method	Material	Re range	Channel dimensions (width × height)	Channel length	Reference
CNC micromilling + assembly	Polycarbonate	1 to 100	[0.4 to 0.6 mm] × 0.4 mm	17.6 mm	19
Soft-lithography + multilayer bonding	PDMS	0.5 to 100	n/r	8 mm	36
Soft-lithography	PDMS	1 to 80	200 μm × n/r	10.2 mm	20
DRIE + glass bonding	Si/glass	0.5 to 100	200 μm × 200 μm	n/r	18
Soft-lithography	PDMS	1 to 220	300 μm × 150 μm	8.5 mm	21
Soft-lithography	PDMS	n/r (200 mm s^{-1})	100 μm × 30 μm	8.75 mm	22
Soft-lithography	PDMS	0.309 to 309	100 μm × 100 μm	40 mm	23
Lamination/Xurography	PVC film	0.1 to 100	700 μm × 70 μm	>13 mm	26
Soft-lithography	PDMS	3.4 to 23.8	500 μm × 150 μm	17 mm	24
Soft-lithography	PDMS	n/r (1.0 to 1000.0 μl min^{-1})	200 μm × 200 μm	6.3 mm	25
Two-photon polymerization + PDMS molding	PDMS	0.01 to 10	100 μm × 100 μm	2 mm	17
SLA 3D printing	Polymer resin	n/r	500 μm diameter	22 mm	37
Soft-lithography	PDMS	0.1 to 45	100 μm × 100 μm	10.51 mm	38
Soft-lithography	PDMS	3.3 to 40	50 μm × n/r	1.5 mm	39
CNC milling and engraving machine	Polycarbonate	1 to 100	400 μm × 400 μm	n/r	40
CNC milling and engraving machine	PMMA	0.5 to 100	200 μm × 200 μm	10.4 mm	41
Layer by layer milling	PMMA, PTFE	25 to 100	800 μm × 800 μm	31.5 mm	42
FDM 3D printing + PDMS molding	PDMS	n/r (60 to 960 μl min^{-1})	200 μm × 300 μm	30 mm	43
Multijet 3D printer	Polymer resin	3.7 to 37.04	500 μm × 400 μm	20 mm	44
Multijet 3D printer	Polymer resin	0.1 to 50	750 μm diameter	20 mm	45
SLA DLP 3D printing	Polymer resin	0.1 to 100	300 μm × 300 μm	10.4 mm	This study

Laminar Flow module was used to simulate single-phase fluid flow in the laminar regime, and the Transport of Diluted Species module was used for modeling the movement of chemical species in a fluid. Detailed settings of the simulation are provided in the SI. To evaluate the homogeneity of mixing across the channel, the mixing efficiency (ME) was calculated using the following expression[29]

$$\mathrm{ME} = 1 - \sqrt{\frac{1}{N}\sum_{i=1}^{N}\left(\frac{c_i - \bar{c}}{\bar{c}}\right)^2}, \quad (1)$$

where c_i is the concentration at the sampling point i over the channel cross-section, N is the total number of sampling points, and $\bar{c}$ is the expected concentration across the channel cross section. The value of ME ranges between 0 and 1, with 1 indicating homogeneous mixing across the channel cross-section.

2.2 Device fabrication

The SAR micromixer and the MCGG with multiple SAR mixing units were 3D printed using Profluidics 285D SLA DLP stereolithography 3D printer (CADWorks3D, Concord, Ontario, Canada). The 3D printer is equipped with a 385 nm wavelength light source and has an XY pixel resolution of 40 μm. While the printer offers high resolution, the actual fidelity of the printed microchannels is highly dependent on the resin properties (such as viscosity and curing characteristics) and the cleaning procedure. In this study, we utilized both Low-viscosity Clear Microfluidics V7.0a, and Cyto-Clear resin (CADWorks3D, Concord, Ontario, Canada). According to the manufacturer, the Cyto-Clear resin is formulated for biocompatibility, though the specific devices reported here were not tested with living organisms. Therefore, the long-term cytotoxicity of the final 3D-printed structures on specific cell lines remains to be fully assessed. It was also noted that printing with the Cyto-Clear resin significantly increased the total fabrication time compared to the standard clear resin. Devices were modeled in SolidWorks Professional 2025 (Dassault Systèmes SolidWorks Corp, Waltham, MA, USA). The models were exported as STL files and imported into the 3D printer software (Utility Software) for slicing. Variable slicing thicknesses of 30 μm and 50 μm were employed. Print and slice detailed parameters are provided in the Supplementary Information. After printing, the devices were first flushed with 90% isopropyl alcohol (IPA) (Cat. #HC5001GAL, Thermo Fisher Scientific Inc., Canada) to remove excess uncured resin and then dried using nitrogen or compressed air. This was followed by a 30-second high-intensity UV post-curing step using the CureZone system (Creative CADWorks, Concord, Ontario, Canada). To ensure experimental consistency and eliminate any risk of cross-contamination or structural degradation between tests, a new device was fabricated for every experiment presented in this study. PTFE tubing with a 1/16″ outer diameter and 1/32″ inner diameter (Cat. #2194272, Cole-Palmer Canada) was connected to the inlets and outlets using super flangeless nuts and ferrules (Cat. #EW-02013-71 and Cat. #0201374, Cole-Palmer Canada).

2.3 SAR micromixer performance evaluation

To visually observe flow behavior in the fabricated SAR micromixers and evaluate their mixing efficiency, we performed two types of optical measurements: wide-field brightfield imaging to assess mixing along the channels, and confocal fluorescence microscopy to evaluate mixing across the channel cross-sections. In the brightfield imaging experiments, sodium hydroxide (NaOH) (Cat. #567530, Sigma Aldrich, Canada) and phenolphthalein (Cat. #470301-998, Ward Science, Canada) in ethanol (70%) (Cat. #HC10001GL, Thermo Fisher Scientific, Canada) were used as the mixing agents. The color change of phenolphthalein, resulting from its reaction with NaOH, was used as an indicator of mixing. A 150 mM NaOH solution in ethanol was introduced through one inlet, and a 10 mM phenolphthalein solution in ethanol was introduced through the second inlet using a dual-channel programmable syringe pump (NE-4000, New Era Pump Systems, New York, United States). The flow rate was incrementally adjusted to achieve Re ranging from 0.1 to 100. For each flow rate, wide-field brightfield images were captured at various positions along the mixing channels of the SAR micromixer using a MRCL700 3D Imager Pro microscope (Microqubic AG, Zug, Switzerland). For the fluorescence microscopy experiments, a 10 μM Fluorescein isothiocyanate–dextran 10 kDa (FITC-10 kDa) (Cat. #FD10S, Sigma Aldrich, Canada) in ultra-pure water was introduced from one inlet, and plain ultra-pure water was introduced through the other. Confocal fluorescence microscopy (Zeiss Laser Confocal LSM 700 with Zeiss Imager M2 Microscope) was used to acquire a z-stack along the height of the channels. Further details on the imaging settings and analysis procedures for the confocal fluorescence microscopy are provided in the SI. Cross-sectional images of the channel at various locations were reconstructed using Zeiss ZEN 3.11 software. To facilitate mounting and optical characterization of NaOH-phenolphthalein and fluorescent solutions, the micromixer footprint was designed to match the dimensions of a standard microscope slide (25 × 75 mm^2). All captured brightfield images were converted to greyscale and analyzed using Python 3.13.2 to calculate the mixing efficiency under varying flow conditions. The mixing efficiency was calculated using the following expression[30,31]

$$\mathrm{ME} = 1 - \sqrt{\frac{1}{N}\sum_{i=1}^{N}\left(\frac{I_{\mathrm{gray},i} - \bar{I}}{\bar{I}}\right)^2}, \quad (2)$$

where $I_{\mathrm{gray}.i}$ is the normalized grayscale intensity at the sampling pixel i, N is the total number of sampling pixels, and $\bar{I}$ is the expected normalized pixel intensity corresponding to the expected concentration. In our experiments, $\bar{I}$ equals to 0.5. To account for spatial variability and reduce the effect of local

intensity outliers, three random transects were extracted from three independent images at each section between mixing units, from top to bottom. The ME was calculated for each transect, and the standard deviation among these values was used to generate the error bars.

Another parameter used to characterize the micromixer is the mixing time at various tested flow rates (corresponding to different Re). We defined complete mixing as ME greater than 0.90, which is consistent with the criterion adopted in previous studies.[17] We then determined the location along the micromixer where this criterion was achieved for each flow rate. The mixing time was then calculated using the following expression

$$\text{Mixing Time} = \frac{V_{\text{straight}}}{2Q_{\text{in}}} + \frac{V_{\text{SAR}}}{2Q_{\text{in}}} \cdot \frac{l_{\text{mix}}}{l_{\text{SAR}}}, \quad (3)$$

where V_{straight} is the volume of the straight section of the mixing channel before the SAR units, Q_{in} is the inlet flow rate, V_{SAR} is the total volume of the SAR units, obtained from the CAD model, l_{SAR} is the axial distance along the straight channel centerline from the input of the first SAR unit to the output of the last SAR unit (*i.e.* the total length of the SAR section along the x-axis), and l_{mix} is the axial distance along the straight channel centerline from the input of the first SAR unit to the location where complete mixing is achieved.

2.4 MCGG performance evaluation

To evaluate the concentration profiles generated by the 3D printed MCGG, a 10 μM FITC-10 kDa solution in ultra-pure water and plain ultra-pure water were introduced through the MCGG's inlets. Fluorescence images of the MCGG channels were captured using a fluorescence microscope (ZEISS Axiovert 5, Carl Zeiss AG, Germany). The images were analyzed using ImageJ to quantify fluorescence intensities at the outlets. Additionally, to assess the MCGG's performance with biomolecules such as proteins, bovine serum albumin (BSA) was used as a model biomolecule. A BSA solution (Cat. #A2934, Sigma Aldrich, Canada) at an initial concentration of 30 μM was introduced into one inlet, while plain ultra-pure water was introduced through the other to establish a concentration gradient at the outlets. From each outlet, 200 μL samples were collected and analyzed in triplicate. BSA concentrations were quantified using Bicinchoninic acid (BCA) protein assay kit (Cat. #71285-M, Sigma Aldrich, Canada) following the manufacturer's protocol. Samples were incubated with the BCA working reagent at 37 °C for 30 minutes. Absorbance was measured at 562 nm using a microplate spectrophotometer (BioTek Epoch 2, Santa Clara, USA), and BSA concentrations were determined by interpolation from a standard calibration curve.

3. Results and discussion

3.1 SAR micromixer design

In most microfluidic applications, the flow in microchannels with smooth walls is laminar, resulting in the mixing of materials between streams occurring purely through diffusion. The time, t_0, required for a solute with diffusion coefficient D to diffuse over a distance l_0 (here l_0 is half-width of the channel) is given by[32]

$$t_0 = \frac{{l_0}^2}{D}. \quad (4)$$

This relationship highlights that the time required for molecular diffusion increases quadratically with the diffusion distance. Split-and-recombine (SAR) micromixers reduce mixing time by repeatedly splitting and recombining flow streams, effectively shortening the length scale over which diffusion must occur. Fig. 1 shows the three-dimensional (3D) model of the designed SAR micromixer, which has been optimized for SLA DLP 3D printing, along with the 3D printed device, more information about the optimization process can be found in the SI. The micromixer comprises eight SAR mixing units, enabling a mixing efficiency above 0.90 for Re ranging from 0.1 to 100. The cross-sectional dimensions of the inlet and outlet channels are 300 × 300 μm^2. The narrowing sections of the SAR units were designed with a minimum width or height of 150 μm. This dimension represents a practical fabrication limit for our SLA DLP setup. Although the printer's XY resolution is 40 μm, we found that attempting to print enclosed channels with dimensions smaller than 150 μm frequently led to clogging or the retention of excess cured resin that could not be effectively removed during the cleaning process. For the dimensions reported in this manuscript, the cleaning procedure was consistently successful in clearing the internal volumes. However, as documented in literature, achieving smaller enclosed features using commercial apparatus remains a significant challenge in 3D-printed microfluidics due to the difficulty of extracting uncured resin from narrow channels.[33]

At each stage, the fluid streams split along the channel height into two sub-streams that flow symmetrically upward and downward. These sub-streams are then geometrically stretched vertically and narrowed horizontally to reach cross-sectional dimensions of 150 μm in width and 300 μm in height. Finally, they are recombined, doubling the number of fluid lamellae. This iterative sequence progressively increases the interfacial area between fluids and reduces the characteristic diffusion length. If l_0 represents the initial diffusion length, the effective diffusion length after n SAR mixing stages becomes

$$l_{\text{SAR}} = \frac{l_0}{2^n}. \quad (5)$$

Consecutively, the required mixing time is reduced to

$$t_{\text{SAR}} = \frac{t_0}{4^n}. \quad (6)$$

This exponential reduction demonstrates the theoretical basis for the SAR strategy's mixing performance. Even a small

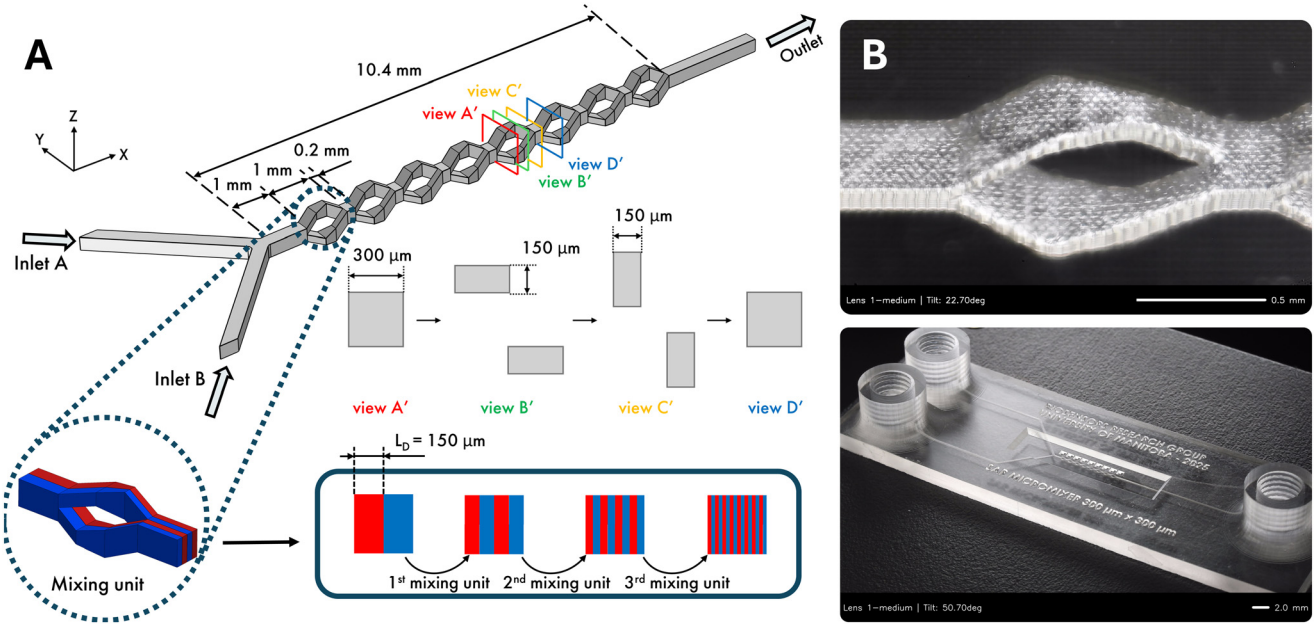

Fig. 1 The designed and fabricated SAR micromixer. (A) The three-dimensional model of the SAR micromixer with a Y-shaped inlet and eight sequential SAR mixing units. The cross-section views A′ to D′ and the inset show fundamental working principle of splitting and recombining mechanism. At each stage, the incoming fluid streams are divided into two sub streams, which are then geometrically reoriented and recombined, effectively shortening the diffusion length scale. (B) Optical image of the 3D-printed SAR micromixer and its mixing units. The device is fabricated by stereolithography digital light processing stereolithography (SLA DLP) 3D printing. The scale bar represents 0.5 mm. The whole device footprint was designed to match a standard microscope slide.

number of stages can reduce the diffusion time by several orders of magnitude.

The final geometry of the SAR micromixer was refined through a systematic investigation of the fabrication constraints associated with the SLA-DLP process to ensure successful monolithic printing and consistent removal of uncured resin. Internal channel widths were selected to allow for the effective clearing of trapped material from the narrowing sections of the SAR units, thereby avoiding internal defects. A specific offset was integrated at the splitting junctions to maintain the structural separation of the channels and prevent them from merging during the printing process. Additionally, a unidirectional arrangement of the units was chosen over an alternating design to encourage a consistent rotational flow that enhances the split-and-recombine mechanism, particularly at higher Re. The architecture also incorporates straight transition sections rather than smooth curves. This geometry promotes stronger reorientation of fluid layers, improving mixing efficiency across a broad range of Reynolds numbers while remaining compatible with the manufacturing capabilities of the printer.

3.2 SAR micromixer simulation and experimental characterization

To assess the practical performance of the designed SAR micromixer beyond its theoretical foundation, numerical simulations and experimental measurements were conducted to evaluate its mixing performance.

Computational fluid dynamics simulations were conducted using COMSOL Multiphysics, as described in section 2.1, for Re ranging from 0.1 to 100. The mixing efficiency was evaluated at multiple positions along the length of the micromixer to quantify the mixing performance after each SAR mixing unit. A baseline simulation of a Y-shaped straight channel, identical in cross-sectional dimensions but without SAR mixing units, was used as a reference to quantify the enhancement in mixing achieved through SAR geometric modulation.

Fig. 2(A) illustrates the concentration distribution along the micromixer and the progressive homogenization after each SAR unit at an inlet flow rate of 9.027 µL min^{-1} corresponding to Re = 1. It is evident that the mixing efficiency increases consistently from unit to unit, highlighting the role of split-and-recombine geometry in enhancing interfacial contact and reducing diffusion length scale. Without the SAR structures, the species travelled the full 10.4 mm with no significant mixing. The quantified simulation results for flow rates from 0.9 to 900 µL min^{-1} (Re 0.1 to 100) are shown in Fig. 2(B). These results indicate that the SAR micromixer achieves complete mixing (ME $>$ 0.90) after eight mixing units, corresponding to a total channel length of 10.4 mm. In contrast, the straight channel exhibited negligible mixing, with the mixing efficiency remaining below 0.25 along its entire length, even at low Re.

To experimentally validate the SAR micromixer, we conducted two independent sets of experiments using a phenolphthalein/NaOH colorimetric assay and fluorescence

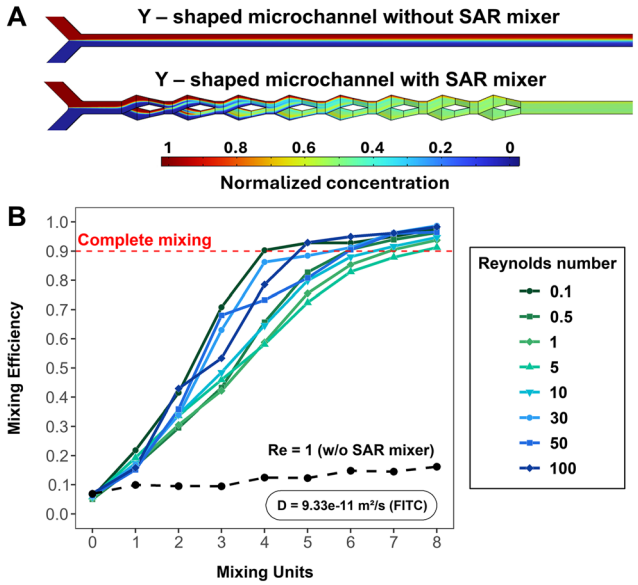

Fig. 2 Simulation results of the SAR micromixer under varying flow conditions. (A) Channel geometry and solute concentration illustrating the mixing dynamics along the channels for Re = 1 and solute diffusion coefficient of $D = 9.33 \times 10^{-11}$ m^2 s^{-1}. The top channel is a straight channel without SAR structures (used as a reference for comparison), while the bottom channel includes eight SAR units. (B) Mixing efficiency *versus* number of SAR mixing units for different Re, ranging from 0.1 to 100. The SAR micromixer achieves progressive mixing with ME > 0.90 after 8 units under all conditions, whereas the straight channel without SAR units exhibits minimal mixing, even at Re = 1.

confocal microscopy of fluorescein isothiocyanate–dextran (FITC-Dextran 10 kDa) in Milli-Q water, as described in section 2.3. Phenolphthalein is a transparent, colorless solution that turns pink in the presence of alkaline conditions, providing a direct visual indicator of the mixing process. Numerical simulations were also performed for each experimental condition, and the corresponding diffusion coefficients of the mixing agents were determined.

Fig. 3(A) shows a side-by-side comparison of the experimental (left column) and simulated (right column) mixing profiles of phenolphthalein and NaOH in ethanol at a flow velocity corresponding to Re = 1. A stable laminar interface is observed from the inlet up to the first SAR unit, indicating minimal initial mixing. As the fluid progresses through the SAR units, the two streams gradually mix, and the resulting pink coloration fills the channel uniformly, with no discernible unmixed streams. This visual uniformity confirms the adequate mixing achieved by the SAR design. The simulated concentration field closely matches the experimental result, supporting the accuracy of the numerical model. Experiments and simulations were performed at flow rates corresponding to Re = 0.1, 0.5, 1, 5, 10, 30, 50, and 100 and the mixing efficiency after the eighth SAR unit was computed using eqn (2). The results presented in Fig. 3(B) show the mixing efficiency (ME) as a function of Re for both the 4th and 8th SAR units. Error bars in Fig. 3(B) represent the standard deviation calculated from three independent images, with three randomly selected transects per image analyzed along the channel, as described in section 2.3. The experimental and simulated data exhibit strong agreement across the entire range of tested Re (0.1–100). Complete mixing (ME > 0.90) is achieved after the final SAR unit (8th) for all conditions. The ME after the 4th unit across the investigated Re range exhibits a non-monotonic relationship between ME and Re, a phenomenon documented in various passive SAR micromixers. In the diffusion-dominated regime (Re < 1), the initial decrease in ME occurs because the residence time within the device is reduced as the flow rate increases, limiting the opportunity for molecular species to diffuse across the fluid interface. This behavior has been previously observed in similar SAR geometries.[17] As Re increases from 1 to 50, the system transitions into an advection-dominated regime. Here, the specific 3D geometry of the mixer forces the fluid to split and recombine while changing planes, which induces centrifugal forces and a rotational component to the flow.[34,35] The temporary decrease in ME observed for Re > 50 is attributed to these rotational flow components counterbalancing the split-and-recombination effect. However, with eight SAR units, the high number of fluid lamellae significantly reduces the diffusion length scale. This ensures that the counteracting balance no longer impacts the overall performance, allowing for rapid homogenization and maintaining a high final ME across the entire Re range. The specific Re values where these transitions occur are specific to our geometry and dimensions. Minor deviations between simulation and experiment are attributed to fabrication imperfections and internal surface roughness, which can affect optical clarity and the accuracy of image-based quantification.

While mixing efficiency offers insight into final mixing quality, it does not reflect how rapidly that state is reached along the length of the micromixer. To capture this, we evaluated the mixing time, defined as the time required for the flow to achieve a mixing efficiency of 0.90 or higher. This was calculated using eqn (3). As shown in Fig. 3(C), the mixing time decreases significantly with increasing Re, from more than 14 seconds at Re = 0.1 to less than 25 milliseconds at Re = 100. Importantly, not all Re require the same number of SAR units to achieve complete mixing. Fewer units are needed at lower Re as the slower flow velocity allows more time for molecular diffusion to occur. In contrast, at higher Re, where residence time is limited and diffusion alone is insufficient, more SAR units are necessary to actively enhance mixing through repeated splitting and recombination.

The internal pressure distribution of the device was calculated through numerical simulations employing the same parameters used for our experimental studies. As detailed in the SI, the simulations predict a maximum pressure drop of approximately 7.5 kPa at Re = 100 across the SAR micromixer under the same conditions used in the experiments. The monolithic 3D-printed architecture accommodated these pressures without leakage or structural failure.

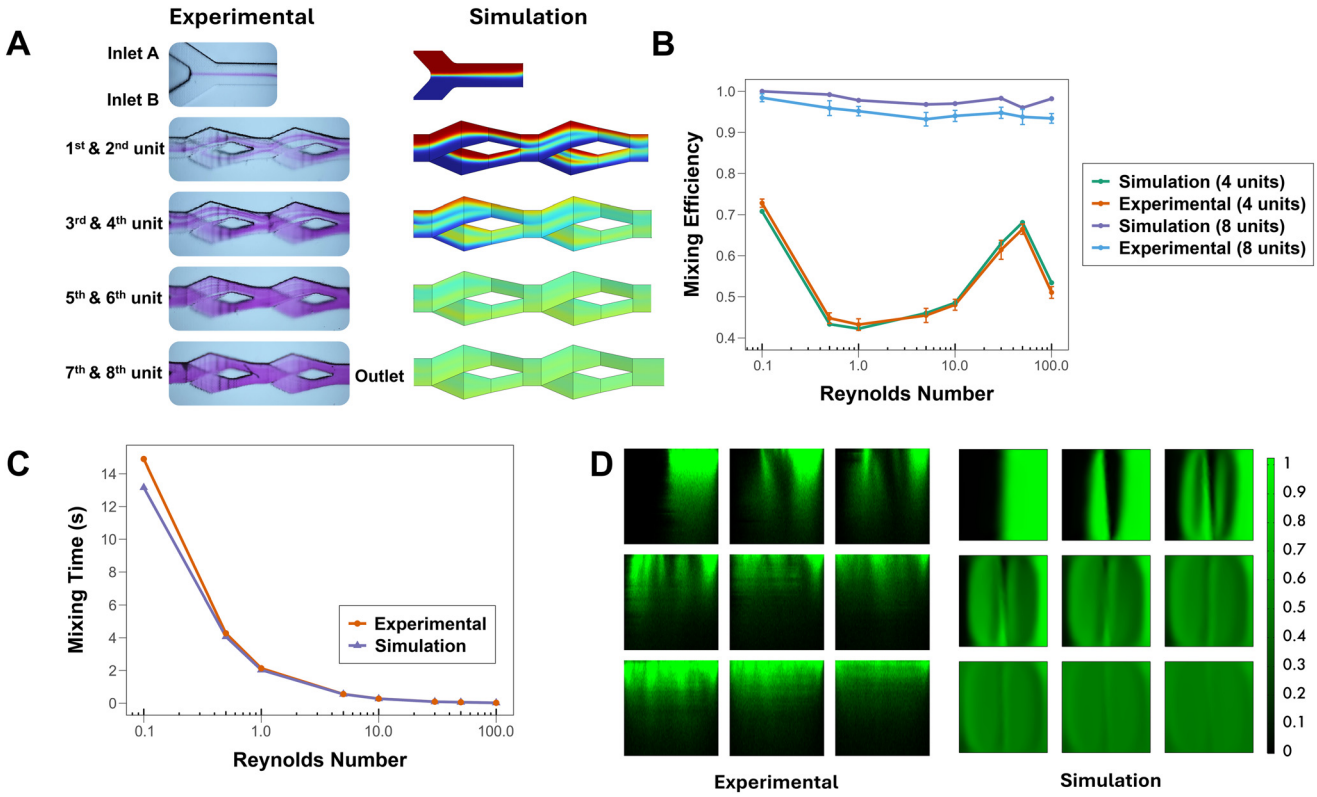

Fig. 3 Experimental and simulated performance of the 3D-printed SAR micromixer. (A) Side-by-side comparison of experimental (left column) and simulated (right column) mixing profiles at Re = 1, using phenolphthalein and NaOH in ethanol as the mixing agents. The uniform pink coloration indicates progressive mixing, consistent with the simulated concentration field. (B) Mixing performance metrics across Re (0.1 to 100) for 4 and 8 SAR units, showing strong agreement between experimental and simulated results and achieving ME $>$ 0.90 across all conditions after 8 units. (C) Corresponding mixing time required to reach ME $>$ 0.90, decreasing from over 14 seconds at low Re to under 0.025 seconds at high Re. (D) Reconstructed fluorescence intensity profiles from nine cross-sections along the SAR micromixer, acquired using confocal laser scanning microscopy with FITC-dextran at Re = 1. The images are arranged in a 3 × 3 matrix from top-left to bottom-right, corresponding to planes captured sequentially from immediately before the first SAR unit to after the eighth SAR unit. Experimental images (left) and simulated cross-sections (right) show progressive homogenization. The lower halves of the experimental images, corresponding to the bottom half of the 300 μm-deep channels, do not show a fluorescent signal due to attenuation through the channel depth and overlying resin, combined with the limited sensitivity of the confocal system.

Fig. 3(D) shows the mixing dynamics of FITC-Dextran 10 kDa in Milli-Q water across nine channel cross-sections, beginning immediately before the first mixing unit and ending after the eighth, as measured by confocal fluorescence microscopy. The left panel images are reconstructed from acquired *z*-stacks along the channel height and depict the fluorescence intensity distribution across the cross-sections. The lower halves of these images, corresponding to the bottom half of the 300 μm-deep channels, do not show a fluorescent signal due to attenuation through the channel depth and overlying resin, combined with the limited sensitivity of the confocal system. Therefore, these results are used primarily for qualitative mechanistic insight, while quantitative validation of homogenization is provided by the rest of experimental analysis and simulations. Based on the top halves, alternating dark and fluorescent streams are observed across the channel width, demonstrating successful split–recombination and progressive homogenization as flow proceeds through the SAR units. In these experiments, the inlet flow rate was set to 9.027 μL min^{-1} (total flow rate of 18.054 μL min^{-1} in the mixing channel, corresponding to Re = 1). The right panel of Fig. 3(D) shows cross-sectional images from computational fluid dynamics simulations using COMSOL Multiphysics. Comparison of the experimental results (top halves of the channels) with the simulations shows good agreement in the dynamics of split–recombination and in the locations of the combined sub-streams.

The results presented in this section confirm that the SAR micromixer achieves high performance across a wide range of flow conditions, with strong agreement between simulations and experimental observations. The ability to achieve complete mixing (ME $>$ 0.90) within eight mixing units for a wide range of Re (0.1 to 100) highlights the effectiveness of the SAR architecture. When compared with previously reported SAR micromixers summarized in Table 1, the present device achieves comparable or higher mixing efficiency while maintaining performance across a broader Re range. Notably, the micromixer was fabricated entirely using desktop SLA 3D printing, demonstrating the feasibility

of producing geometrically complex internal structures without the need for cleanroom facilities or multistep microfabrication processes. Despite its three-dimensional design, the micromixer can be easily and rapidly fabricated, tested, and iteratively refined within a single working day, enabling fast prototyping and performance optimization. These capabilities make it ideally suited for integration into more advanced microfluidic systems. In the following section, we demonstrate the incorporation of this 3D-printed SAR micromixer into a multi-output microfluidic concentration gradient generator (MCGG), designed to produce five distinct, well-defined concentrations at discrete outlets for chemical and biological applications.

3.3 Microfluidic concentration gradient generator design

The designed and 3D-printed microfluidic concentration gradient generator (MCGG) (shown in Fig. 4) features two fluidic inlets and five discrete outlets. The design has a tree-shaped network with a SAR micromixer at each branch. In this architecture, concentration gradients are generated by sequential concentration division at interconnected nodes. A key consideration in the design of the MCGG is the type of mixing required at different stages of the network. In the primary and secondary branches (Fig. 4(B)), mixing at intermediate nodes is not intended to be complete; instead, it is sufficient to achieve an equal average concentration between the incoming streams. For this reason, each mixing module in these branches contains only two SAR units. At the tertiary branches leading to the outlets, complete mixing is required to ensure homogeneous solutions are collected at the outlets. For this reason, each mixing module in the tertiary branches contains eight SAR units. This staged mixing strategy, utilizing SAR micromixers, enables us to achieve five thoroughly mixed concentrations with a smaller footprint. The designed MCGG can be analyzed based on the concept of hydraulic circuit theory, which is analogous to electrical networks (Fig. 4(B)). With two inlets operating at equal flow rates and input concentrations of $C_A = 0$ and $C_B = 1$, and assuming symmetric channel resistances, sequential mixing is expected to produce normalized outlet concentrations of 0, 0.25, 0.5, 0.75, and 1 at the five outlets. The total internal volume of the integrated MCCG-SAR system is approximately 20 μL. While this volume may be limiting for certain low-volume biomedical applications, it is well suited for high-throughput chemical mixing in agricultural and environmental settings, where operational working volumes are substantially larger. This internal volume represents a design optimization to prevent channel occlusion during the 3D-printing process, balancing sample consumption with reliable manufacturability.

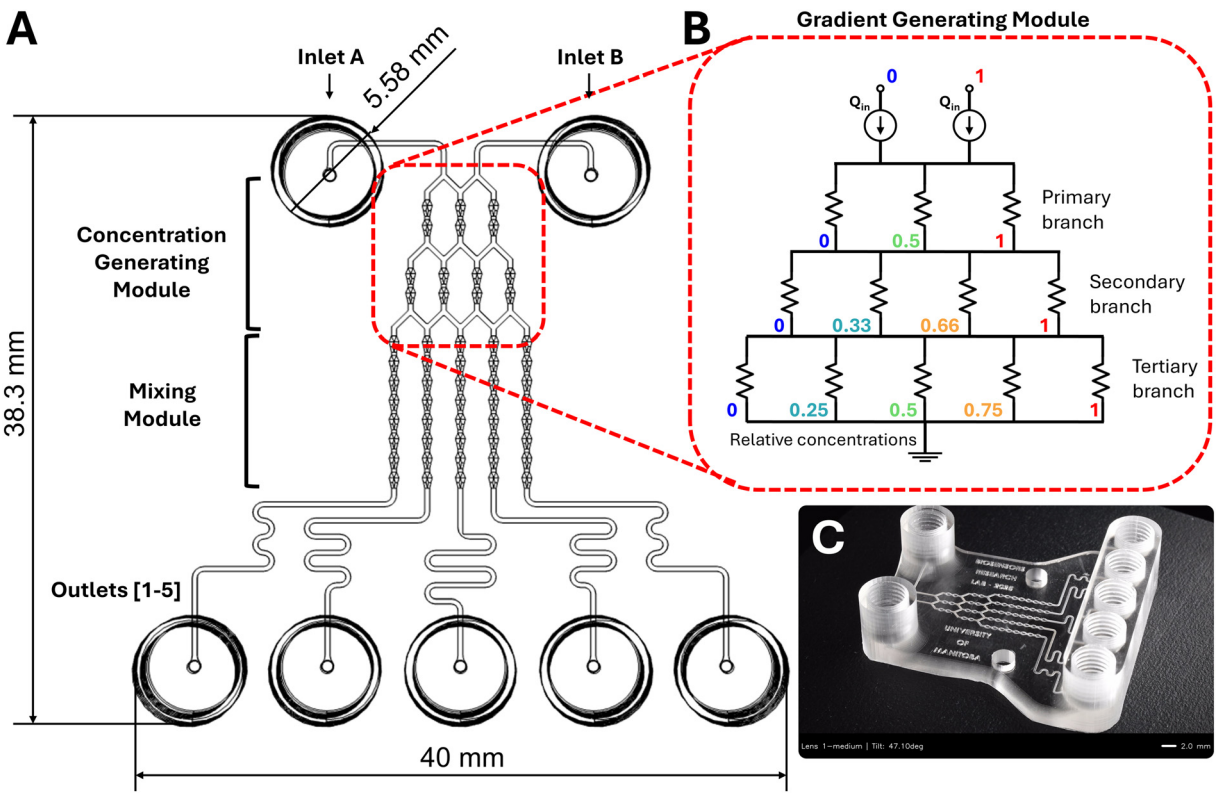

Fig. 4 Design and operation principle of the 3D-printed MCGG with integrated SAR micromixers. (A) Schematic drawing of the MCGG. (B) Electrical circuit analogy of the MCGG. Full concentration ($C = 1$) and zero concentration ($C = 0$) samples are introduced into inlets A and B at the same flow rate. Colored numbers represent the relative concentrations of each node. (C) The 3D printed MCGG. The embedded channels and SAR structures are visible through the transparent resin. Scale bar represents 2 mm.

In addition to the microfluidic network, the system includes 3D-printed functional modules such as threaded fluidic ports, Luer-lock adapters, and a sample collector compatible with standard microcentrifuge tubes. These components were integrated seamlessly during the design phase and fabricated simultaneously using SLA DLP 3D printing (Fig. 5), demonstrating the versatility of the approach in producing both micro- and macro-scale features for plug-and-play microfluidic systems.

3.4 3D MCGG simulation and characterization

To evaluate the performance of the 3D-printed microfluidic concentration gradient generator (MCGG), we conducted a combined study involving numerical simulations and experimental characterization across a wide range of flow conditions. The MCGG integrates a network of channels with embedded SAR mixing units to produce five discrete, well-defined output concentrations from two input streams.

Simulations were performed using the Laminar flow and transport of diluted species modules in COMSOL Multiphysics. The model predicted progressive concentration division at key internal nodes and complete mixing at the outlet, even under low Re regimes. When two input solutions with relative concentrations of 0 and 1 were introduced, the simulated outlet values matched the target profile of 0, 0.25, 0.5, 0.75, and 1.0. To assess the accuracy of intermediate mixing, normalized concentrations were evaluated at three critical nodes, located within the primary and secondary branches where splitting and recombination occur. While complete mixing is not required at the internal nodes, the incorporation of two SAR units is essential to achieve the correct average concentration delivered to the subsequent stage. By introducing two SAR units, the fluid layers are geometrically split and recombined, providing a symmetrical average concentration between the right and left halves of the cross-section, independent of local mixing efficiency. This ensures that the two split subsections deliver the intended intermediate concentrations to the next division channels, therefore maintaining the gradient accuracy. A simple straight channel cannot achieve this behavior, as the absence of transverse transport would cause the left and right halves of the cross-section to retain their initial unmixed concentrations (approximately 0 and 1). As shown in Fig. 6(A), the average concentration of the right and left halves of each cross-sectional plane at these nodes (nodes 1, 2, and 3) closely followed the theoretical values of 0.33, 0.50, and 0.66, respectively, across a range of Re. This confirmed that the designed network reliably achieved predictable intermediate concentrations prior to final mixing.

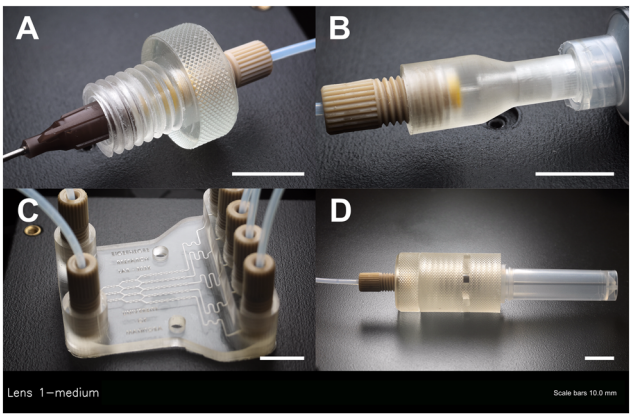

Fig. 5 3D-printed functional modules integrated into the MCGG system. (A) 1/4-28 UNF (unified fine, a thread standard) to male Luer-lock adapter for syringe needle. (B) 1/4-28 UNF to female Luer-lock adapter for syringe (C) gradient generator with threaded 1/4-28 UNF inlet and outlet ports. (D) Sample collector base compatible with 1.5 mL microcentrifuge and assembled system showing the integration of the fluidic components with standard lab hardware. These elements were fabricated using the same SLA DLP 3D printing workflow, highlighting the feasibility of manufacturing both microfluidic networks and functional macro components in a single process. Scale bars represent 10 mm.

Fig. 6(B) presents the simulated cross-sectional profiles at the same three critical nodes at a representative flow rate of 90.27 μL min^{-1} (corresponding to Re = 5), illustrating the lamellar distribution and progressive interfacial development at internal mixing points. The final outlet concentrations, evaluated as the average cross-sectional concentration at each outlet, are shown in Fig. 6(C). The results exhibit consistent output gradients of 0, 0.25, 0.5, 0.75, and 1.0 across all simulated flow rates, confirming the validity of the MCGG design under low and high Re conditions. This stability highlights a key advantage of the integrated SAR nodes: the resulting gradient is governed by the device architecture and volumetric balancing rather than the diffusion time.

To experimentally evaluate the performance of the designed MCCG, FITC-Dextran 10 kDa was dissolved in ultrapure water and introduced through one inlet, while Milli-Q water was introduced through the other. The experimental results, shown in Fig. 7(A, left), captured the dynamic formation of concentration lamellae and progressive dilution within the device, closely resembling the simulated profiles (Fig. 7(A), right). The SAR structures effectively split and recombined flow streams, confirming their functional role in gradient formation. Quantification of fluorescent intensity at the outlets was analyzed through the image analysis procedure described in section 2.4. Normalized outlet concentrations were obtained from the averaged fluorescence intensities measured at each outlet channel. The error bars in Fig. 7(B) represent the standard deviation derived from three random transects analyzed along the channel, as described in section 2.4. The fluorescence-based analysis yielded a coefficient of determination (R^2) of 0.9984 relative to the simulation data, confirming the high reproducibility and accuracy of the experimental gradient generation.

A separate evaluation using bovine serum albumin (BSA) as a model macromolecule was performed to assess the generator's performance with biomolecules of lower diffusivity. As described in section 2.4, outlet samples were

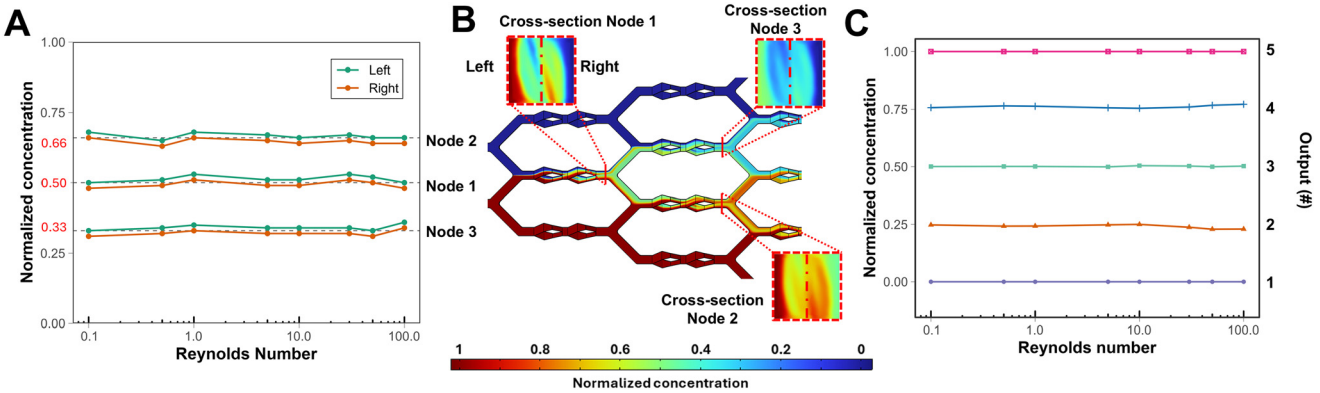

Fig. 6 Simulation-based characterization of critical nodes and outlet gradients in the 3D-printed MCGG. (A) Normalized concentration values at each cross-sectional plane of three critical nodes (nodes 1, 2, and 3) across a range of Re (0.1–100), calculated from the average of the right and left halves. Red values indicate the expected theoretical concentrations based on ideal concentration division (*e.g.*, 0.33, 0.50, 0.66), confirming the MCGG's ability to maintain predictable concentration ratios across flow regimes. (B) Simulated cross-sectional concentration profiles at three critical nodes at a representative flow rate of 90.27 μL min^{-1} (Re = 5), illustrating the lamellar distribution at internal mixing points. (C) Normalized concentration values at the five discrete outlet channels, plotted across all simulated Re. Results show consistent and stable output gradients (0, 0.25, 0.5, 0.75, 1.0) for all simulated flow rates, confirming the performance of the MCGG design in low and high Re conditions.

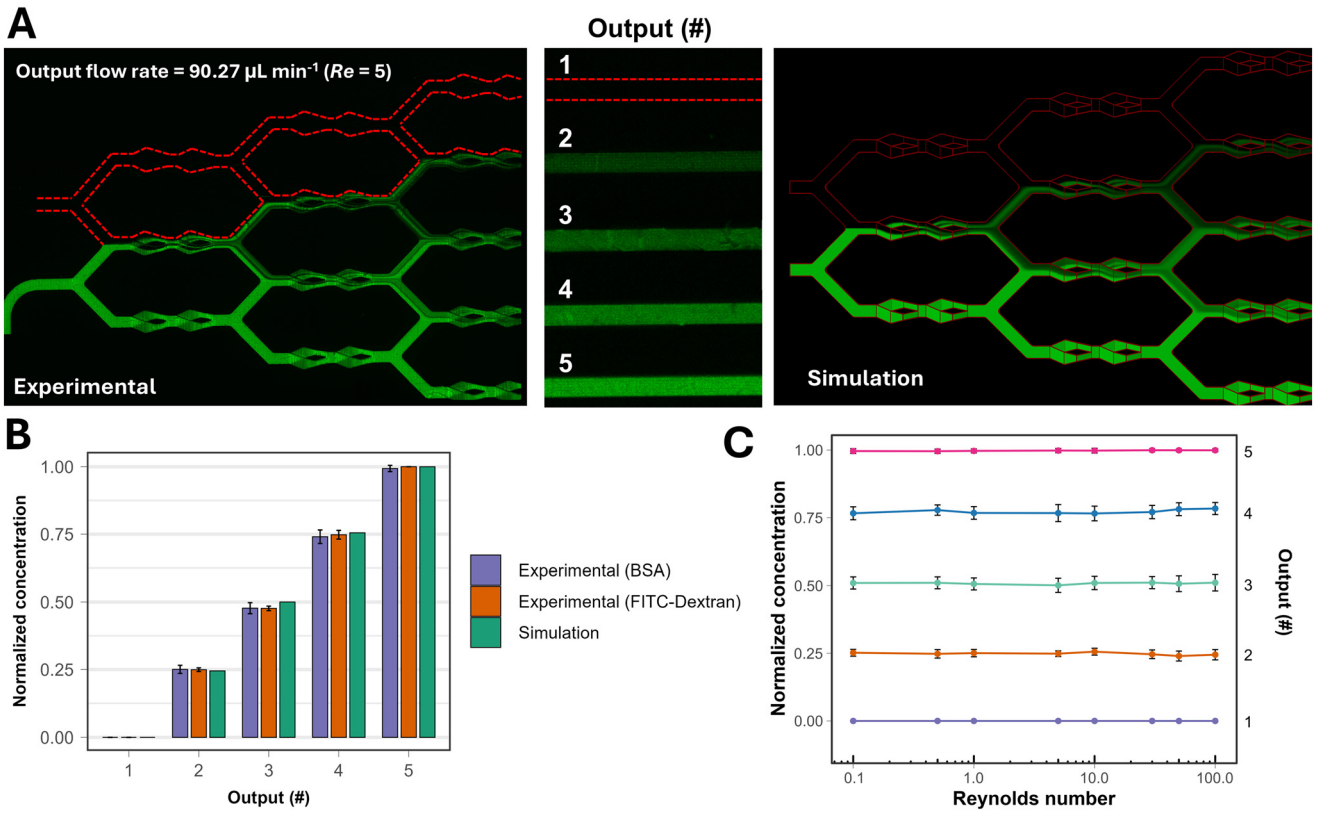

Fig. 7 Experimental validation of the SAR-based 3D-printed MCGG using fluorescent tracers. (A) Side-by-side comparison of experimental (left) and simulated (right) concentration distributions at a flow rate of 90.27 μL min^{-1} (Re = 5), using FITC–Dextran and Milli-Q water as inputs. The experimental images capture the expected progression of splitting, recombination, and dilution throughout the gradient network. The central panel shows the fluorescence image of the five outlet channels, visually confirming the formation of stable and distinct concentration levels consistent with the designed output gradient. (B) Quantitative comparison of normalized concentrations at the five output channels between simulation and experimental results. Experimental validation was conducted using FITC-Dextran, detected *via* fluorescence microscopy, and BSA, quantified through a bicinchoninic acid (BCA) assay to verify the accuracy of the concentration gradient generator at a flow rate of 90.27 μL min^{-1} (Re = 5). Both experimental datasets closely follow the simulated profile, with high coefficients of determination (R^2 = 0.9984 for FITC and 0.9972 for BSA), confirming the gradient generator's ability to reproducibly generate discrete concentrations with both small molecules and proteins. (C) Normalized concentration values at the five discrete outlet channels, plotted across all tested Re. Results show consistent and stable output gradients (0, 0.25, 0.5, 0.75, 1.0) for all experimentally tested flow rates, confirming the performance of the MCGG design in low and high Re conditions.

collected and analyzed using the bicinchoninic acid (BCA) assay. Each BSA concentration value represents the average of triplicate measurements obtained by spectrophotometric analysis, with error bars indicating the corresponding standard deviation. The quantified BSA concentrations (Fig. 7(B)) followed the expected stepwise gradient, showing excellent correlation with the simulated values, with a coefficient of determination (R^2) of 0.9972. These results confirm that the MCGG can reliably generate well-defined and reproducible concentration gradients for both fluorescent tracers and protein solutions.

Fig. 7(C) represents the experimentally measured normalized concentrations, obtained from fluorescence intensities at each outlet, across Re from 0.1 to 100. The results show five consistent output levels that closely match the expected gradient values (0, 0.25, 0.5, 0.75, and 1.0), confirming that the MCGG maintains stable and reproducible gradients over the full range of tested flow conditions. These results validate the SAR-integrated MCGG as a reliable platform for rapid generation of discrete concentration gradients under laminar flow conditions. The system consistently delivers target outputs, at various flow rates, enabled by both the hydraulic resistor network and the enhanced interfacial mixing provided by the SAR architecture.

Compared with existing microfluidic gradient generators, our design emphasizes a compact 3D-printed architecture, SLA DLP-enabled rapid prototyping, and precision output control through embedded SAR units. Together, these results highlight the potential of low-cost, cleanroom-free SLA DLP 3D printing to enable next-generation microfluidic platforms for the reproducible and scalable generation of chemical gradients.

4. Conclusion

In this study, we presented the design, simulation, and experimental characterization of a fully monolithic stereolithography digital light processing (SLA DLP) 3D-printed split-and-recombine (SAR) micromixer integrated within a microfluidic concentration gradient generator (MCGG). The device effectively generates five discrete, stable, and reproducible concentrations with high mixing performance (ME $>$ 0.90) across a wide Re range (0.1–100). The high efficiency observed across these three orders of magnitude is a result of the architectural preservation of the SAR mechanism. Computational fluid dynamics (CFD) simulations and experimental measurements demonstrated excellent agreement, confirming the reliability of both the SAR geometry and the fabrication approach.

The proposed cleanroom-free process enables the rapid production of optically transparent, enclosed microchannels and integrated ports in a single fabrication step, reducing total production time to under 1.5 h using a desktop SLA DLP printer. This workflow eliminates molds and bonding steps, simplifying the transition from digital design to functional microfluidic devices. The demonstrated mixing performance and gradient reproducibility highlight the potential of SLA DLP additive manufacturing as an accessible method for fabrication of such microfluidic systems.

Overall, this work establishes an efficient and versatile route for the rapid prototyping of lab-on-a-chip devices that integrate advanced micromixing strategies and gradient generation.

Author contributions

Francisco Navarro (writing—original draft, investigation, data curation, formal analysis), Elham Salimi (conceptualization, investigation, supervision, writing—review & editing, resources, project administration), and Jitendra Paliwal (conceptualization, supervision, writing—review & editing, resources).

Conflicts of interest

The authors declare no conflicts of interest.

Data availability

All relevant data supporting the findings of this study are provided in the electronic supplementary information (SI), including the CAD models of the device and videos of the pH-based mixing and fluorescence experiments. Additional datasets are available upon reasonable request. Supplementary information is available. See DOI: https://doi.org/10.1039/d5lc01095k.

Acknowledgements

This work was supported by the Natural Sciences and Engineering Research Council of Canada (NSERC), Mitacs, Saskatchewan Pulse Growers, and the Canada Foundation for Innovation (CFI).

References

1 A. K. Au, W. Huynh, L. F. Horowitz and A. Folch, *Angew. Chem., Int. Ed.*, 2016, **55**, 3862–3881.
2 N. Bhattacharjee, A. Urrios, S. Kang and A. Folch, *Lab Chip*, 2016, **16**, 1720–1742.
3 G. Comina, A. Suska and D. Filippini, *Lab Chip*, 2014, **14**, 2978–2982.
4 A. I. Shallan, P. Smejkal, M. Corban, R. M. Guijt and M. C. Breadmore, *Anal. Chem.*, 2014, **86**, 3124–3130.
5 S. Waheed, J. M. Cabot, N. P. Macdonald, T. Lewis, R. M. Guijt, B. Paull and M. C. Breadmore, *Lab Chip*, 2016, **16**, 1993–2013.
6 Y. Guo, Z. Gao, Y. Liu, S. Li, J. Zhu, P. Chen and B.-F. Liu, *Anal. Chem.*, 2020, **92**, 12062–12070.
7 B. Hong, P. Xue, Y. Wu, J. Bao, Y. J. Chuah and Y. Kang, *Biomed. Microdevices*, 2016, **18**, 21.
8 J. El-Ali, P. K. Sorger and K. F. Jensen, *Nature*, 2006, **442**, 403–411.

9 A. G. G. Toh, Z. P. Wang, C. Yang and N.-T. Nguyen, *Microfluid. Nanofluid.*, 2014, **16**, 1–18.
10 N.-T. Nguyen and Z. Wu, *J. Micromech. Microeng.*, 2005, **15**, R1–R16.
11 A. D. Stroock, S. K. W. Dertinger, A. Ajdari, I. Mezić, H. A. Stone and G. M. Whitesides, *Science*, 2002, **295**, 647–651.
12 S. Huang, Y. Wu, Y. Wang, X. Hu and K. Song, *Electrophoresis*, 2024, **45**, 420–432.
13 S. Zhang, Y. Han, T. Lacassagne, N. Cagney, C. P. Naveira-Cotta, S. Balabani and M. K. Tiwari, *Chem. Eng. Sci.*, 2023, **267**, 118349.
14 B. Lee, M. Kim, S. Oh, D. Bi Lee, S.-G. Lee, H. Min Kim, K. H. Kim, J. Song and C.-S. Lee, *Chem. Eng. Sci.*, 2023, **281**, 119161.
15 W. Raza, N. Islam and A. Samad, *Chem. Eng. Process.*, 2023, **183**, 109246.
16 X. Qi, J. Wang, C. Chen and L. Wang, *Chem. Eng. Process.*, 2024, **196**, 109677.
17 Z. Wang, X. Yan, Q. Zhou, Q. Wang, D. Zhao and H. Wu, *Anal. Chem.*, 2023, **95**, 8850–8858.
18 X. Chen, J. Shen and Z. Hu, *Sens. Rev.*, 2018, **38**, 321–325.
19 V. Viktorov, C. Visconte and M. Readul Mahmud, *J. Fluids Eng.*, 2016, **138**, 091201.
20 X. He, T. Xia, L. Gao, Z. Deng and B. B. Uzoejinwa, *Micro Nano Lett.*, 2019, **14**, 293–298.
21 A. Fuwad, S. Hossain, H. Ryu, M. A. Ansari, M. S. I. Khan, K.-Y. Kim, T.-J. Jeon and S. M. Kim, *Chem. Eng. Technol.*, 2020, **43**, 1866–1875.
22 X. Zhang, Z. Qian, M. Jiang, W. Li, Y. Huang and Y. Men, *Micromachines*, 2022, **13**, 1720.
23 C.-H. D. Tsai and X.-Y. Lin, *Micromachines*, 2019, **10**, 583.
24 S. Zhu, Y. Fang, Y. Chen, P. Yu, Y. Han, N. Xiang and Z. Ni, *Int. J. Heat Mass Transfer*, 2022, **183**, 122129.
25 S. Sivashankar, S. Agambayev, Y. Mashraei, E. Q. Li, S. T. Thoroddsen and K. N. Salama, *Biomicrofluidics*, 2016, **10**, 034120.
26 R. A. Taheri, V. Goodarzi and A. Allahverdi, *Micromachines*, 2019, **10**, 786.
27 V. Karamzadeh, A. Sohrabi-Kashani, M. Shen and D. Juncker, *Adv. Mater.*, 2023, **35**, 2303867.
28 A. Naderi, N. Bhattacharjee and A. Folch, *Annu. Rev. Biomed. Eng.*, 2019, **21**, 325–364.
29 L.-H. Lu, K. S. Ryu and C. Liu, *J. Microelectromech. Syst.*, 2002, **11**, 462–469.
30 H. Fu, X. Liu and S. Li, *RSC Adv.*, 2017, **7**, 10906–10914.
31 F. Mahmud and K. F. Tamrin, *Asia-Pac. J. Chem. Eng.*, 2020, **15**, e2407.
32 H. Bruus, *Theoretical microfluidics*, Oxford Univ. Press, Oxford, 2011, Reprinted with corr.
33 C. T. Desire, R. D. Arrua, B. Michalatos, J. Zhang, X. L. Venn, M. Breadmore, Z. Kopecki, N. McMillan, R. Fitridge, E. F. Hilder and A. J. Cowin, *Anal. Chim. Acta*, 2026, **1384**, 344971.
34 M. A. Ansari, K.-Y. Kim, K. Anwar and S. M. Kim, *J. Micromech. Microeng.*, 2010, **20**, 055007.
35 V. Viktorov, R. Mahmud and V. Carmen, MCM, 2015.
36 G. Liu, M. Wang, L. Dong, D. Zhu, C. Wang, Y. Jia, X. Li and J. Wang, *Sens. Actuators, A*, 2022, **341**, 113569.
37 K. Plevniak, M. Campbell, T. Myers, A. Hodges and M. He, *Biomicrofluidics*, 2016, **10**, 054113.
38 A. B. Ghosh and A. Atta, *Ind. Eng. Chem. Res.*, 2023, **62**, 4135–4150.
39 Y. Liao, Y. Mechulam and B. Lassalle-Kaiser, *Sci. Rep.*, 2021, **11**, 20119.
40 V. Viktorov, M. R. Mahmud and C. Visconte, *Eng. Appl. Comput. Fluid Mech.*, 2016, **10**, 182–192.
41 X. Chen and J. Shen, *Anal. Methods*, 2017, **9**, 1885–1890.
42 Y. Ma, Y. Zhao, T. Su, X. Li, L. Yang and Y. Zhao, *J. Micromech. Microeng.*, 2025, **35**, 045007.
43 D. Koo and H. So, *Sci. Rep.*, 2022, **12**, 6346.
44 A. Enders, I. G. Siller, K. Urmann, M. R. Hoffmann and J. Bahnemann, *Small*, 2019, **15**, 1804326.
45 E. C. Sweet, R. Mehta, Y. Xu, N. Liu, K. Korner, C. C. Glick and L. Lin, in *2019 20th International Conference on Solid-State Sensors, Actuators and Microsystems & Eurosensors XXXIII (TRANSDUCERS & EUROSENSORS XXXIII)*, IEEE, Berlin, Germany, 2019, pp. 2258–2261.

